

## **Supplementary information**

High power densities created from salinity differences by  
combining electrode and Donnan potentials in a concentration  
flow cell

Taeyoung Kim, Bruce E. Logan, and Christopher A. Gorski\*

Department of Civil and Environmental Engineering, The Pennsylvania State University,  
University Park, PA 16802, USA

\*Corresponding Author: [gorski@engr.psu.edu](mailto:gorski@engr.psu.edu);

+1-814-865-5673 (phone), +1-814-863-7304 (Fax)

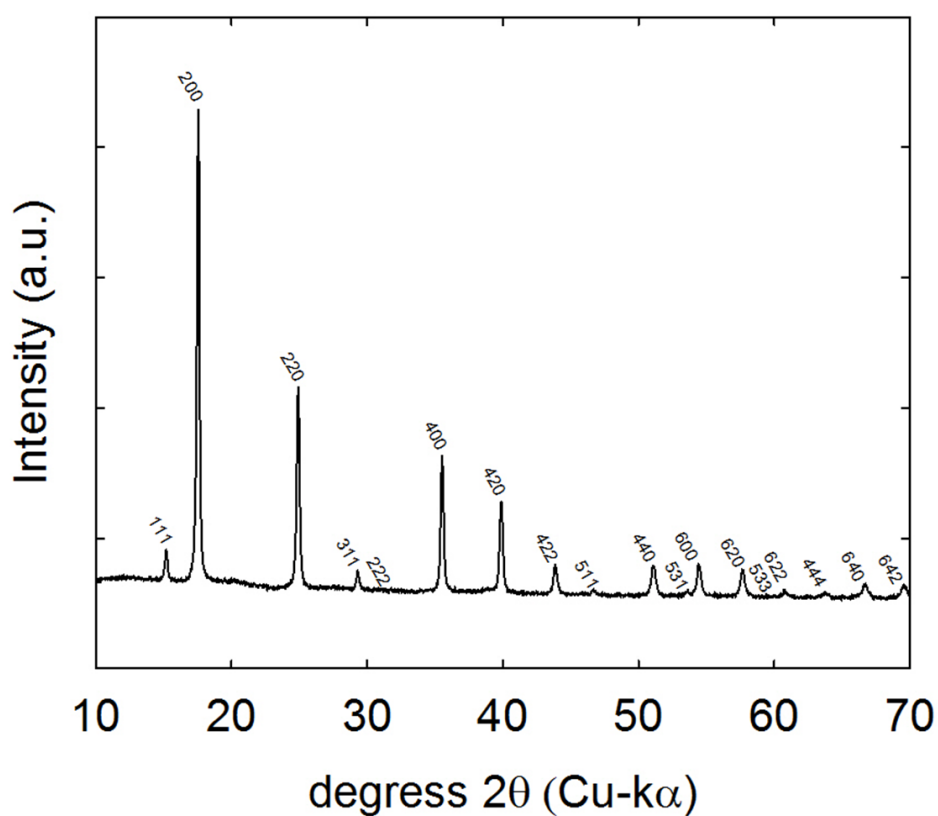


**Figure S1.** X-ray diffraction (XRD) pattern of CuHCF. The pattern was obtained by using a PANalytical Empyrean X-Ray Diffractometer in the scan range between 10 and 70 degrees  $2\theta$  with a Cu  $k\alpha$  source. The XRD pattern shows a typical crystalline structure of CuHCF, in good agreement with a previously reported XRD pattern for CuHCF prepared using the same co-precipitation method.<sup>1</sup>

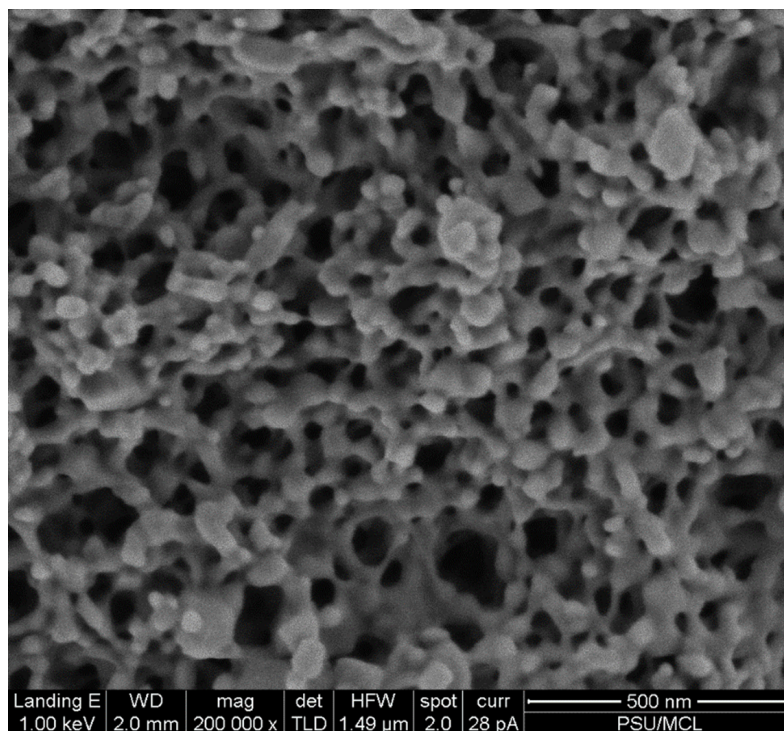


**Figure S2.** A representative scanning electron microscope (SEM) image of the CuHCF sample. The image was collected using a Nova NanoSEM 630 (FEI Corporation, Hillsboro, OR).

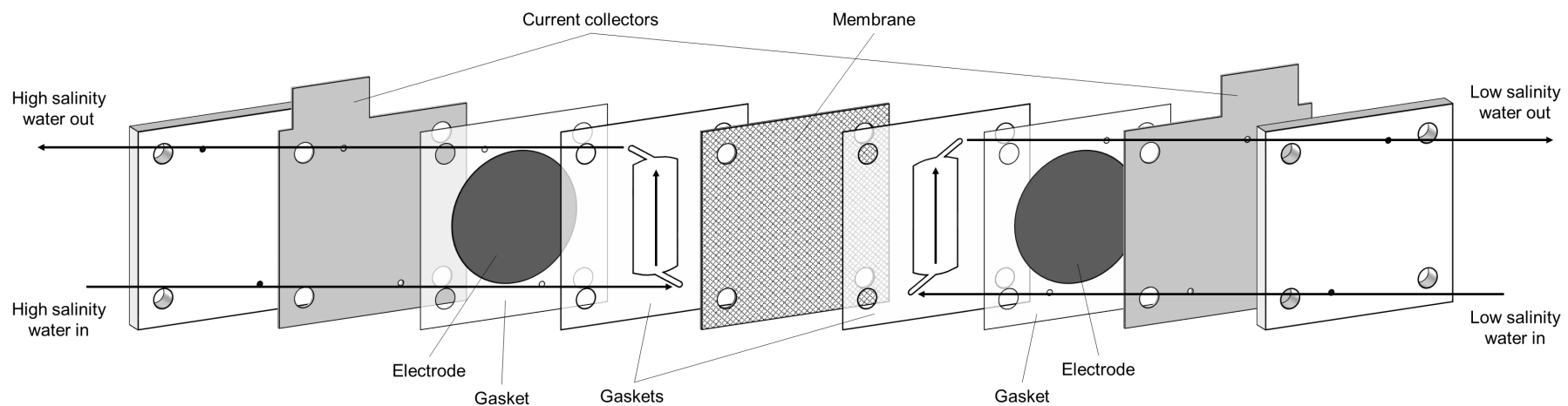


**Figure S3.** A schematic of a custom-built flow cell.

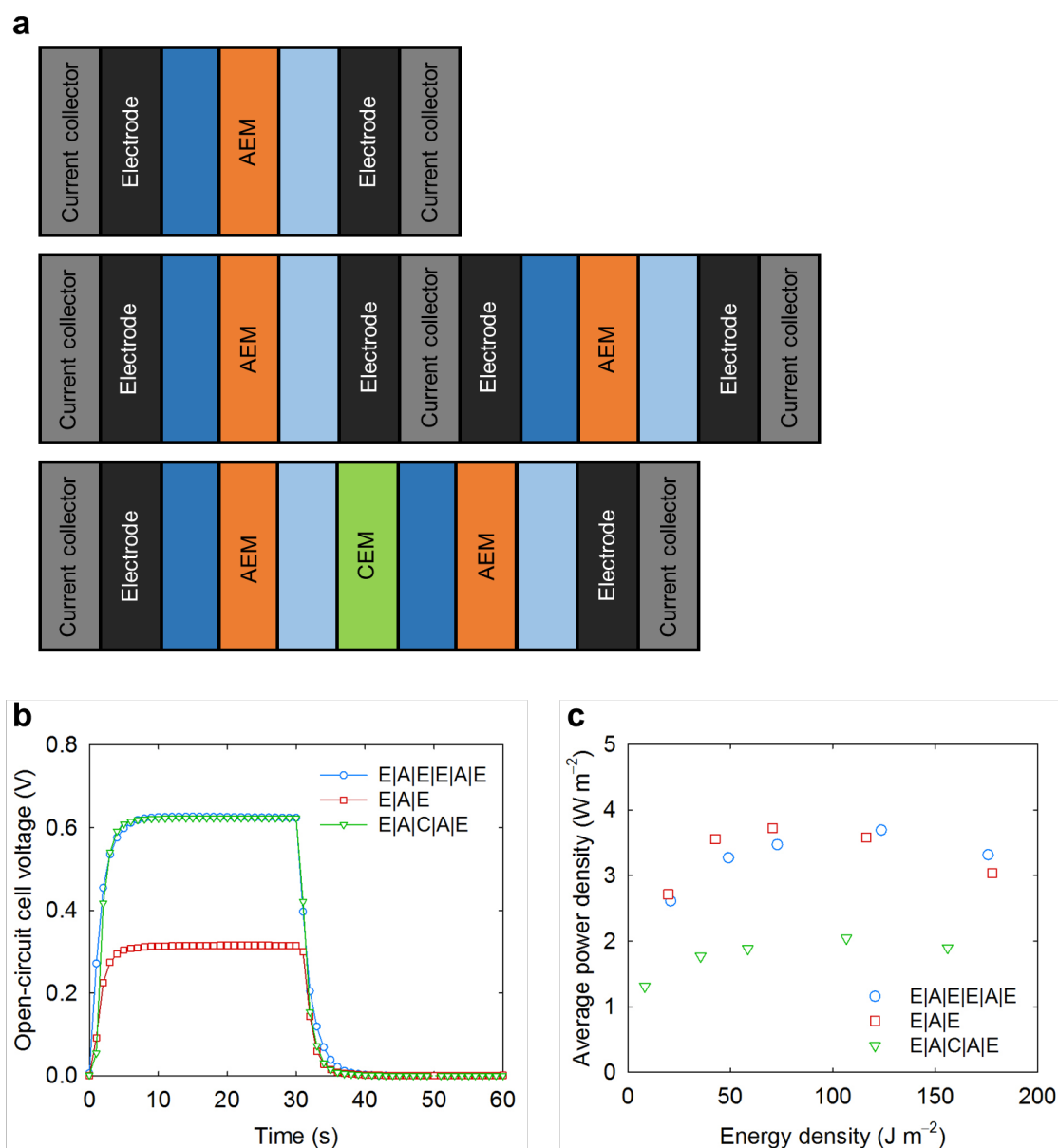


**Figure S4.** (a) Schematic of single (E|A|E), double- (E|A|E|E|A|E), and membrane-stacked (E|A|C|A|E) cells, where E indicates the electrode, A the anion-exchange membrane, and C the cation-exchange membrane. (b) Open-circuit cell voltage profiles, and (c) average power density vs. energy density plot for different cell configurations.

### Supplementary Note 1. Evaluating energy efficiency

To evaluate the energy efficiency (i.e., the ratio of energy extracted to energy available from two solutions with different concentrations) we calculated the available energy by following equation:<sup>2</sup>

$$\Delta G_{mix} = RT \sum_i [c_{i,h} V_h \ln(c_{i,h}) + c_{i,l} V_l \ln(c_{i,l}) - c_{i,m} V_m \ln(c_{i,m})]$$

where  $\Delta G_{mix}$  is the difference in the Gibbs free energy of mixing (J),  $c$  is the concentration (M),  $R$  is the gas constant ( $8.314 \text{ J mol}^{-1} \text{ K}^{-1}$ ),  $T$  is the temperature (298 K),  $V$  is the volume (L), subscript  $h$  is the high salt concentration solution, subscript  $l$  is the low salt concentration solution, and subscript  $m$  is the mixed solution. The available energy when mixed 1:1 volume ratio of high concentration (0.513 M) and low concentration (0.017 M) NaCl solutions was 0.724 kJ per liter of the mixed solution (Fig. S5).

We then evaluated the energy obtained experimentally from the HC and LC solutions by using the concentration flow cell. Since the system was not yet optimized to maintain two effluent solutions separated in each reservoir during the operation, the obtainable energy was calculated based on several assumptions and experimental results. First, we evaluated the minimum volume needed to gain the cell voltage from the salinity difference by recording open-circuit cell voltages depending on the flow rate. The equilibrium cell voltage was attained more rapidly as the flow rate increased (Fig. S6a). When plotted the volume used to reach approximately 0.3 V as a function of the flow rate, less volume was needed as the flow rate decreased (Fig. S6b). From the y-intersect value of the fitted line, the minimum volume needed was found to be 0.73 mL for each solution. This value was approximately 20 times more than that of each channel (0.036 mL), and was used to calculate the obtainable energy per volume of the mixed solution (1.46 mL).

To calculate the experimental extracted energy from a given salinity difference and the volume, we discharged the concentration flow cell by applying constant current without flowing the solutions. The amount of energy harvested depended on the applied current, yielding higher energy recoveries at lower currents (Fig. S7a). We measured the recoverable energy at the lowest current (0.5 mA) using several combinations of HC and LC solutions (Fig. S7b). The empirical equation derived from two plots (Figs. S7c and d) allowed us to estimate the energy extracted and the concentration of each solution per cycle. The sum of the energy extracted from multiple cycles until two solutions were completely mixed was the experimentally obtainable energy ( $0.534 \text{ kJ L}^{-1}$ ), and dividing this by the theoretically available energy ( $0.724 \text{ kJ L}^{-1}$ ) resulted in the energy efficiency of 73.8%. This energy efficiency accounted for release/uptake of  $\text{Na}^+$  ions by CuHCF electrodes and  $\text{Cl}^-$ -ion transport through the anion-exchange membrane.

In additional inefficiency we accounted for was due to the periodic switching of solutions. Specifically, when the solutions were switched, residual solution could remain on a side of the cell when the new solution is introduced. This magnitude of this effect accounted for by considering the volume of solution that absorbed inside the electrode, which was porous. A term ' $r$ ' was used to define the ratio of the volume of the void inside the electrode to that of the flow channel (0.036 mL). A higher  $r$  value indicates the more solution absorbed in the electrode and the more unwanted mixing, thus the energy efficiency decreased as  $r$  increased (Fig. 6a), and the concentration changed accordingly (Fig. 6b). Realistic values for  $r$  were obtained using  $\text{N}_2$  adsorption isotherm (Micromeritics ASAP 2420, Fig. S8a) and mercury intrusion porosimetry (Micromeritics AutoPore V Model 9620, Fig. S8b). For these analyses, the CuHCF electrode was cut into small pieces including the substrate (carbon cloth)

and the other components (carbon black and polymer binder). The use of N<sub>2</sub> adsorption isotherm allowed for measuring volume of pores between 1.7 and 300 nm, which yielded the pore volume of 0.07 cm<sup>3</sup> g<sup>-1</sup> (BJH desorption). The use of mercury intrusion porosimetry allowed for measuring volume of pores between 0.003 and 360 μm, which yielded the pore volume of 1.86 cm<sup>3</sup> g<sup>-1</sup>. Note that in the case of the mercury intrusion porosimetry measurement, a high applied pressure (60,000 psi) might have produced overestimated pore volume, because a part of the CuHCF electrode was flexible carbon cloth. The mass of the CuHCF exposed to the flow channel (~ 3 cm<sup>2</sup>) was approximately 0.05 g, which was used to calculate the electrode pore volume for each analysis. The pore volume measured using N<sub>2</sub> adsorption isotherm produced  $r = 0.09$ , and the mercury intrusion porosimetry produced  $r = 2.53$ , indicating that accounting larger pores resulted in more energy loss caused by solutions trapped inside the CuHCF electrode.



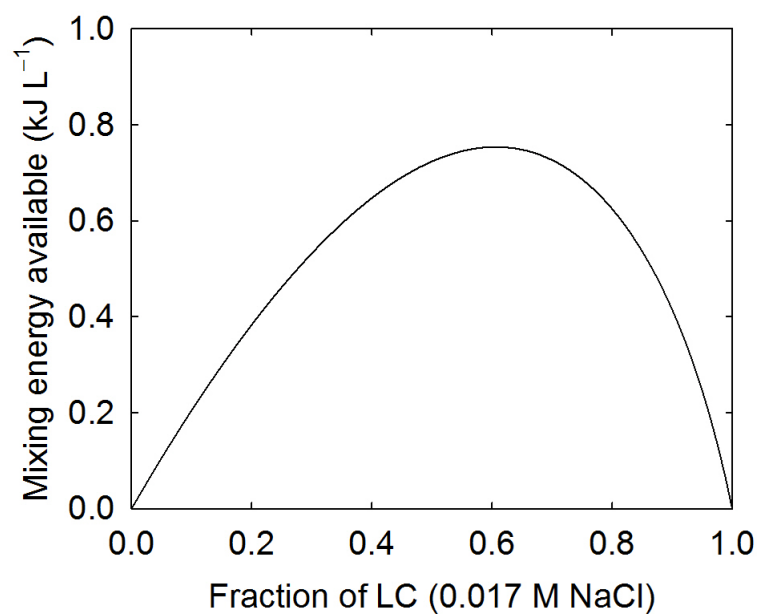


**Figure S5.** Theoretically available energy (kJ per liter of the mixed solution) when mixing high concentration (HC, 0.513 M) and low concentration (LC, 0.017 M) NaCl solutions, depending on the fraction of the LC solution.

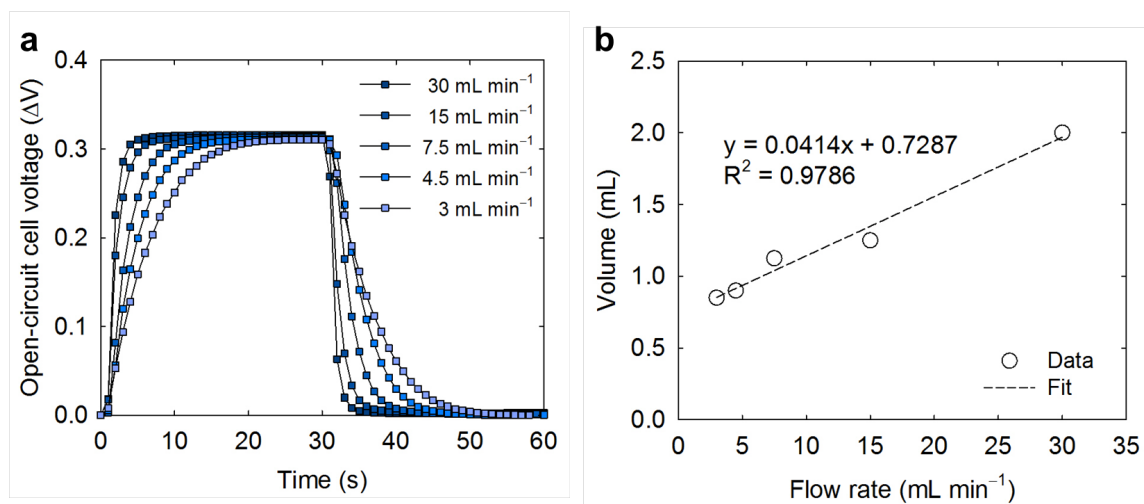


**Figure S6.** (a) Open-circuit cell voltage profiles as a function of the flow rate. (b) Volume needed vs. flow rate plot.

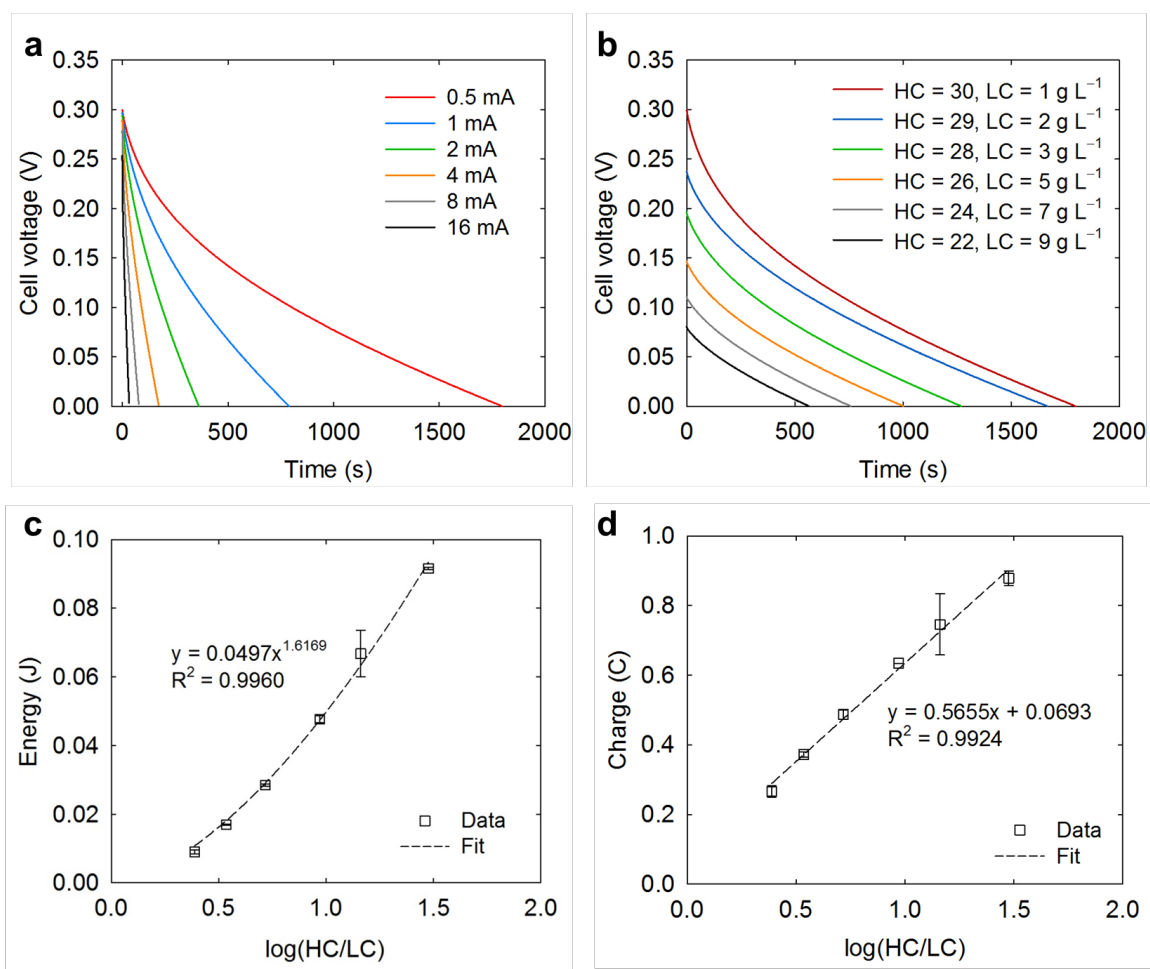


**Figure S7.** (a) Cell voltage profiles vs. time depending on the applied current in the concentration battery cell filled with high concentration (HC, 30 g L<sup>-1</sup>) and low concentration (LC, 1 g L<sup>-1</sup>) solutions and (b) depending on the HC and LC solutions at 0.5 mA. (c) Energy vs. log(HC/LC) and (d) Charge vs. log(HC/LC) plots that were derived by calculating energy and charge from the each pair of HC and LC solutions.

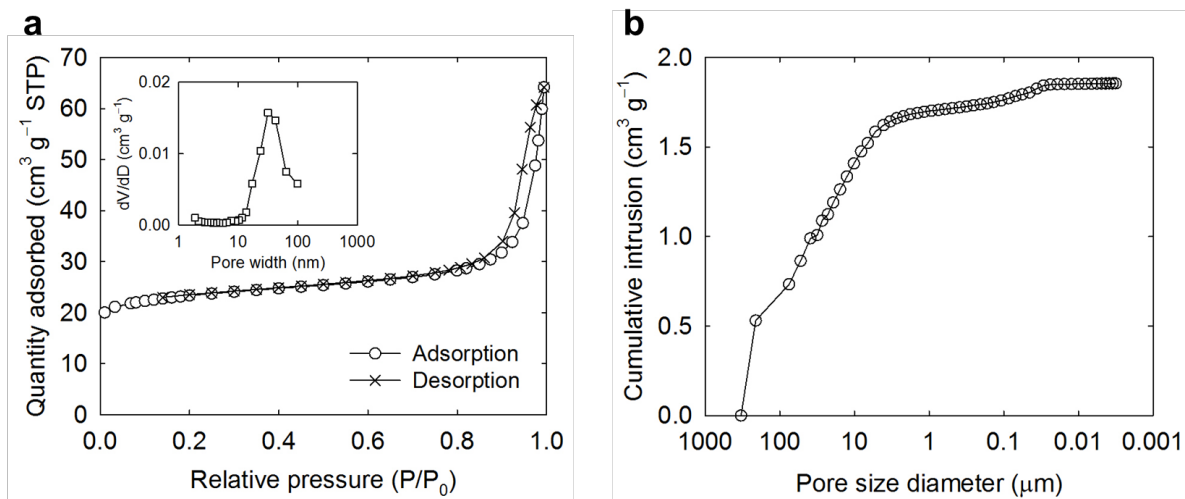


**Figure S8.** (a) Nitrogen adsorption isotherm and (b) mercury intrusion porosimetry. Analyses were performed using electrode pieces consisting of the CuHCF, carbon black, binder, and carbon cloth current collector.

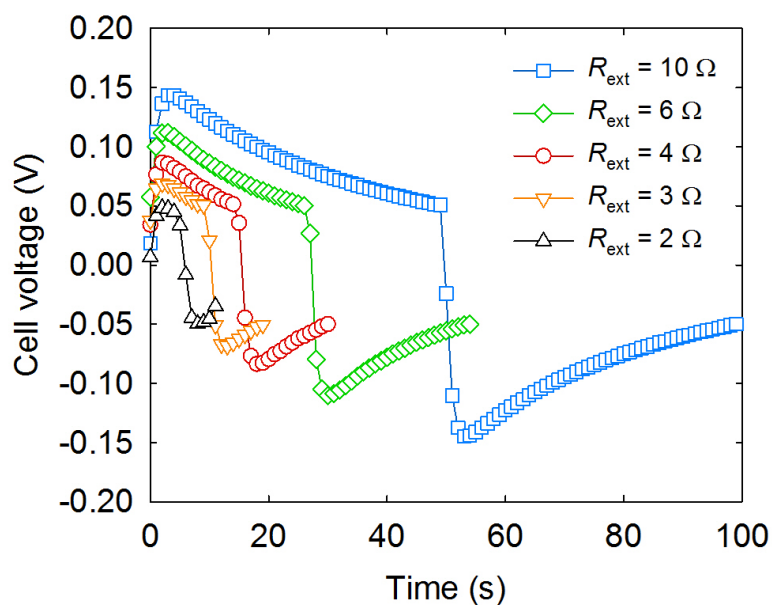


**Figure S9.** Representative cell voltage profiles as a function of the load ( $R_{\text{ext}} = 2, 3, 4, 6, 10 \Omega$ ). High ( $30 \text{ g L}^{-1}$ ) and low concentration ( $1 \text{ g L}^{-1}$ ) solutions were fed to each channel at the flow rate of  $15 \text{ mL min}^{-1}$ , and the flow path of the solutions was switched when the cell voltage decreased below  $\pm 0.05 \text{ V}$ .

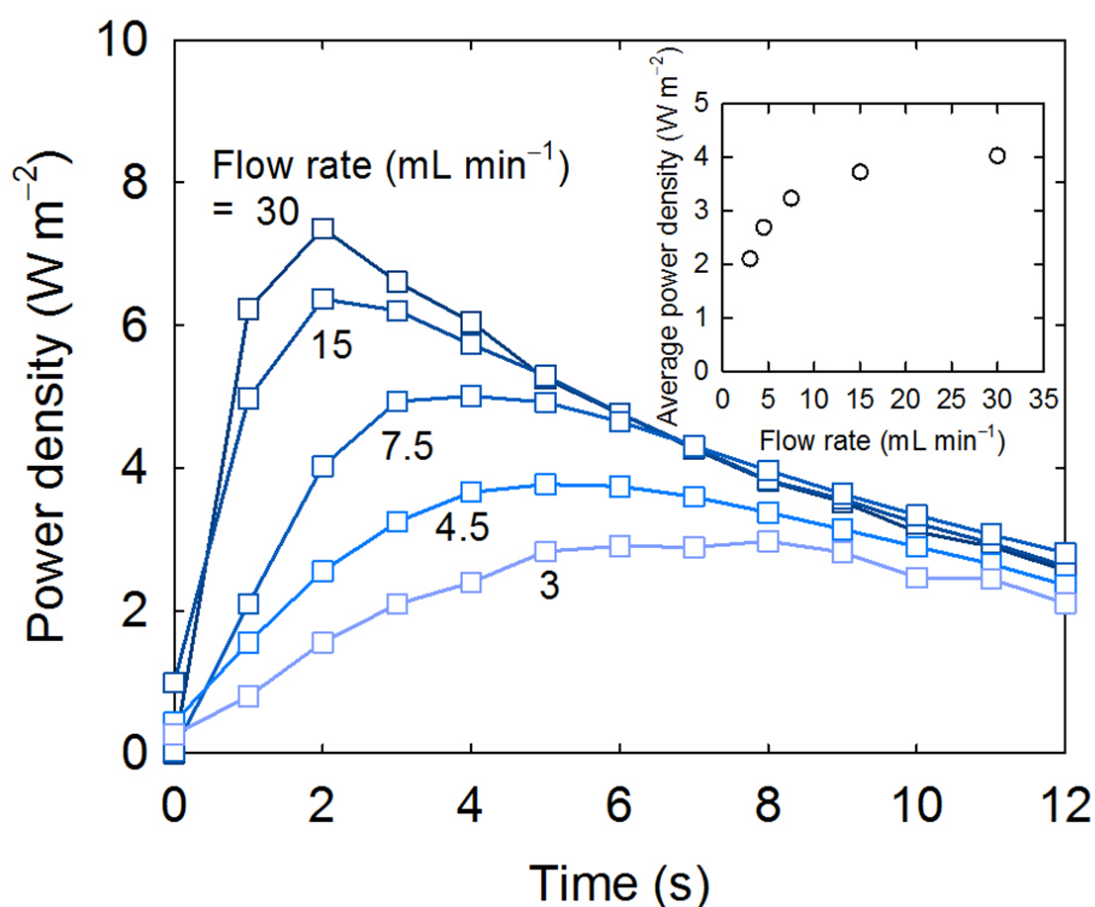


**Figure S10.** Effect of the flow rate on power density and average power density (inset). The flow rates of the high ( $30 \text{ g L}^{-1}$ ) and low concentration ( $1 \text{ g L}^{-1}$ ) solutions were adjusted to be between 3 to  $30 \text{ mL min}^{-1}$  ( $R_{\text{ext}} = 4 \Omega$ ). Both power and average power productions were strongly dependent on the flow rate. The use of a higher flow rate allowed for rapid solution exchange between high and low concentration solutions, and therefore the electrode could rapidly develop the concentration-dependent potential, leading to a high power density. The flow rate of  $15 \text{ mL min}^{-1}$  would be the optimal condition when considering a balance between maximizing power densities and minimizing energy losses due to pressure drops and pumping energy.

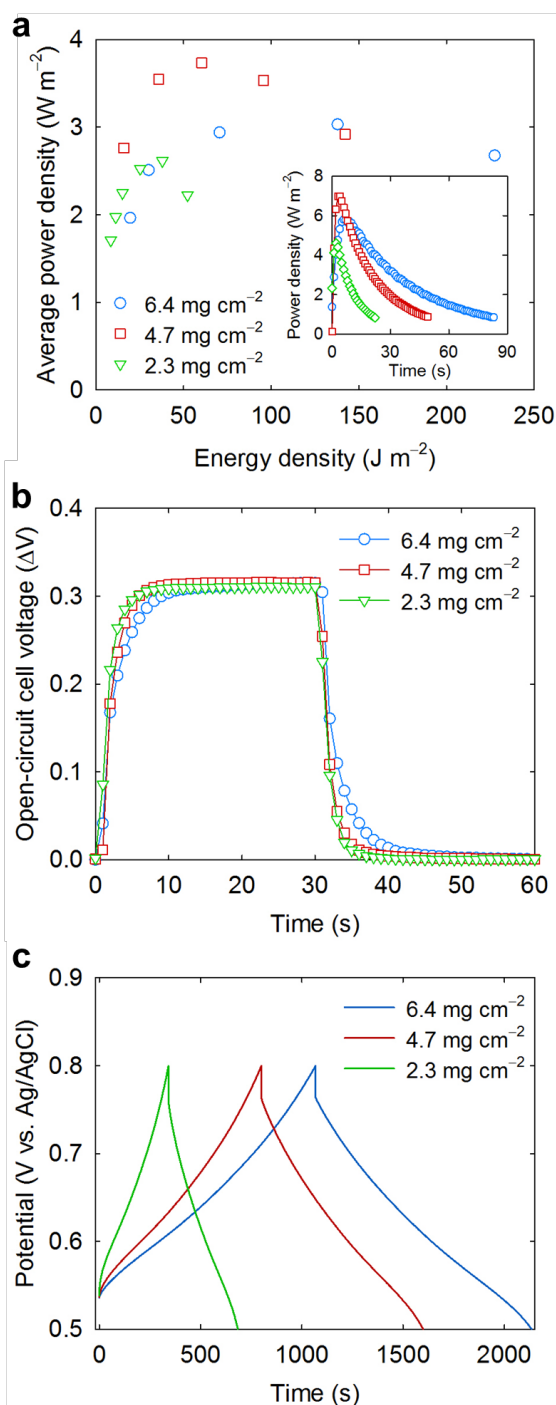


**Figure S11.** (a) Average power density vs. energy density plots depending on the electrode mass loading. Each plot was obtained as a function of the load ( $R_{\text{ext}} = 2, 3, 4, 6, 10 \Omega$ ). High ( $30 \text{ g L}^{-1}$ ) and low concentration ( $1 \text{ g L}^{-1}$ ) solutions were fed to each channel at the flow rate of  $15 \text{ mL min}^{-1}$ . Time-dependent power densities were calculated at  $R_{\text{ext}} = 10 \Omega$  (inset). (b) Open-circuit cell voltage profiles and (c) galvanostatic cycling tests ( $5 \text{ mA}$ ) as a function of the electrode mass loading.

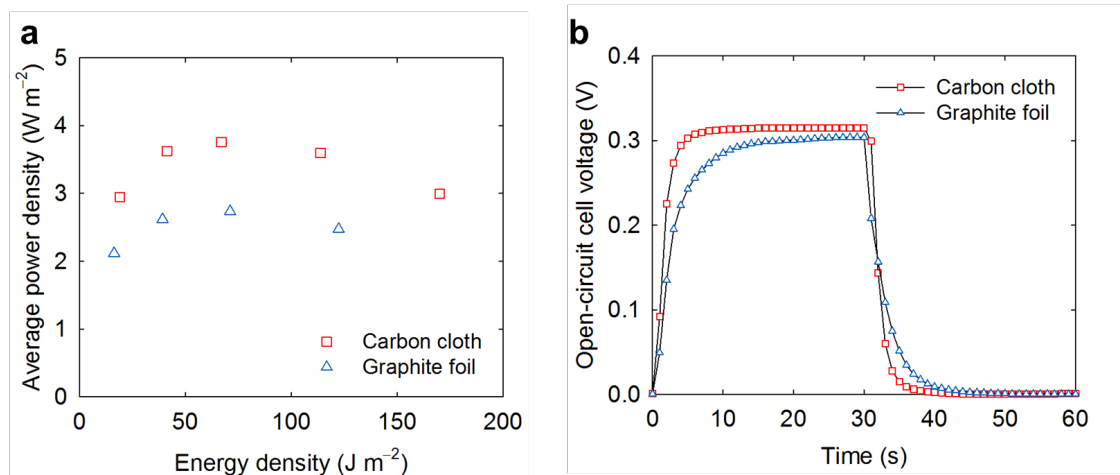


**Figure S12.** (a) Average power density vs. energy density plots with different substrates used for fabricating electrodes. Each plot was obtained as a function of the load ( $R_{\text{ext}} = 2, 3, 4, 6, 10 \, \Omega$  for carbon cloth;  $R_{\text{ext}} = 3, 4, 6, 10 \, \Omega$  for graphite). High ( $30 \, \text{g L}^{-1}$ ) and low concentration ( $1 \, \text{g L}^{-1}$ ) solutions were fed to each channel at the flow rate of  $15 \, \text{mL min}^{-1}$ . (b) Open-circuit cell voltage profiles of CuHCF electrodes fabricated onto carbon cloth and graphite foil.



## **Supplementary Note 2. Open-circuit cell voltage profiles of the concentration flow cell using a non-selective membrane**

To examine the role of a non-selective membrane in the concentration flow cell, we measured open-circuit cell voltages with and without CuHCF electrodes. When we used NaCl solutions (note that these are also shown in [Fig. 3b](#)), the open-circuit cell voltage of the flow cell with CuHCF electrodes (0.185 V) was slightly higher than the calculated value based on activities (0.162 V), and this was due to the contribution of the non-selective membrane that provided a small potential (0.037 V). This increase can partly be explained by a small junction potential that was created across the membrane, because  $\text{Cl}^-$  diffuses faster than  $\text{Na}^+$  from high to low salt concentration solutions<sup>3</sup>. When we used KCl solutions, however, the concentration flow cell contained only the non-selective membrane developed similar open-circuit cell voltages, even though  $\text{K}^+$  and  $\text{Cl}^-$  have similar diffusion coefficients that should result in no junction potential ([Fig. S13](#)). It seems likely that the non-selective membrane aided the selective transport of  $\text{Cl}^-$ , which behaved similar to an anion-exchange membrane, and therefore produced a small Donnan potential.

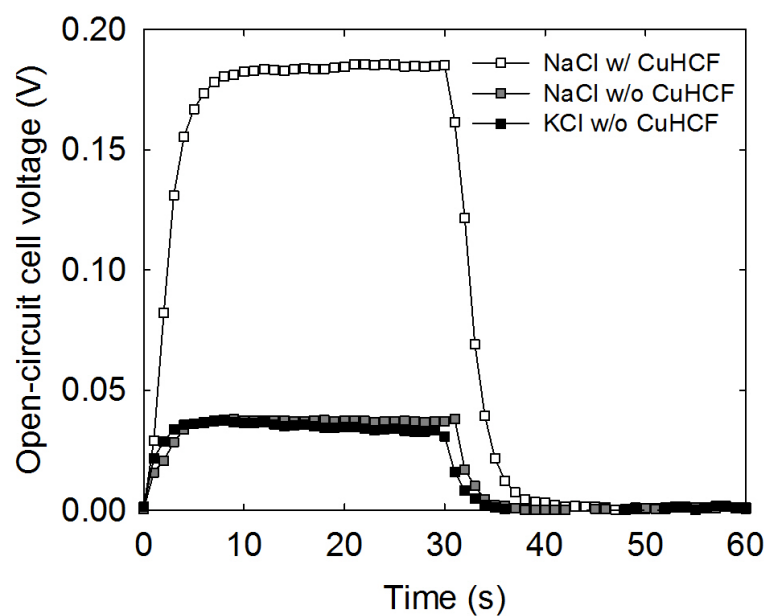


**Figure S13.** Open-circuit cell voltage profiles of the concentration flow cell containing a non-selective membrane w/ and w/o CuHCF electrodes.

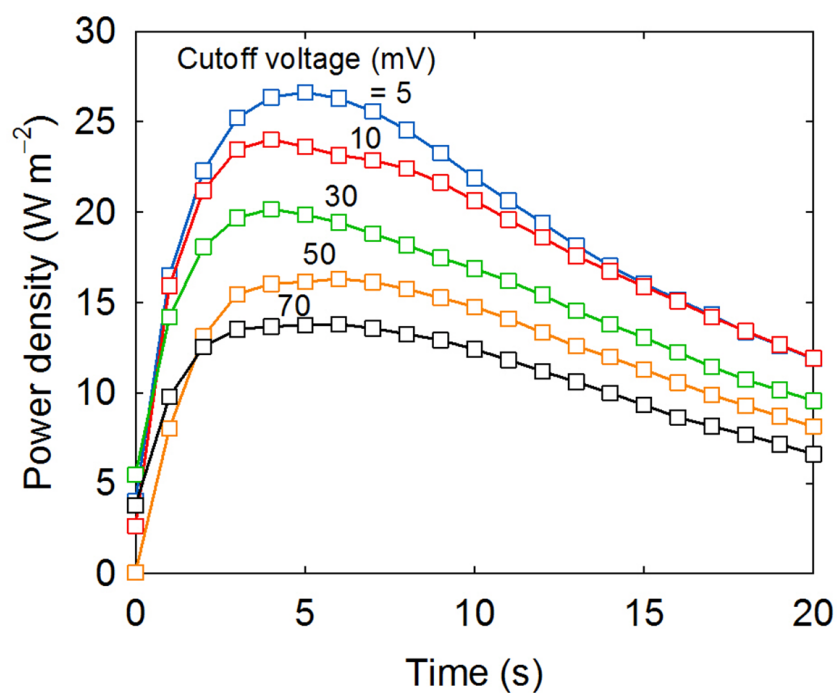


**Figure S14.** Power density profiles as a function of cutoff voltage using 1 and 300 g L<sup>-1</sup> NaCl solutions. The external resistor placed between two electrodes was 6  $\Omega$ . Adjusting discharge frequency affected the power production because a longer discharge (a lower cutoff voltage) developed a higher cell voltage in the following cycle. A lower cutoff voltage produced a higher peak power density, while there was a tradeoff between peak and average power densities.

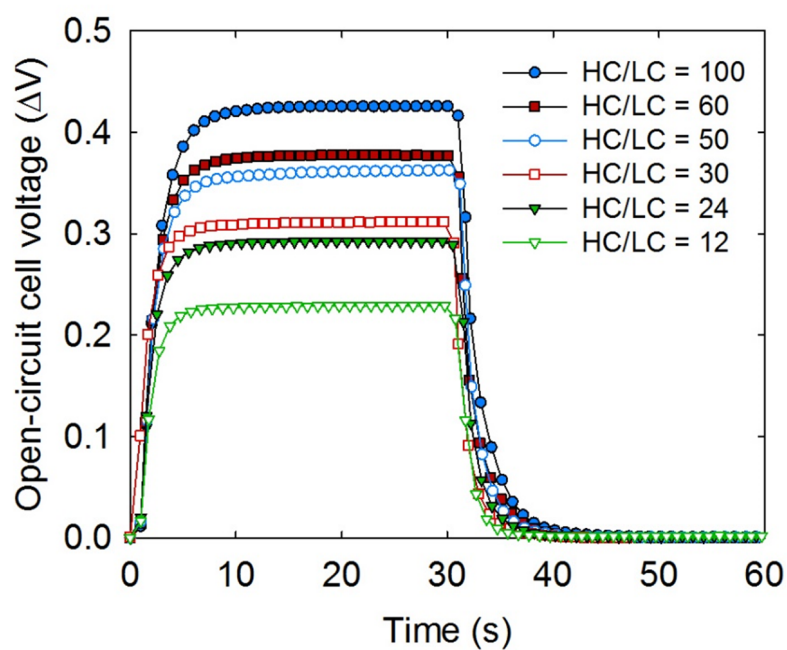


**Figure S15.** Open-circuit cell voltage profiles depending on the ratio of high concentration ( $HC = 30, 60 \text{ g L}^{-1}$ ) to low concentration ( $HC = 0.6, 1, 2.5 \text{ g L}^{-1}$ ) solutions. The flow rate was  $15 \text{ mL min}^{-1}$  for each solution, and the flow path between the solutions was switched every 30 sec.

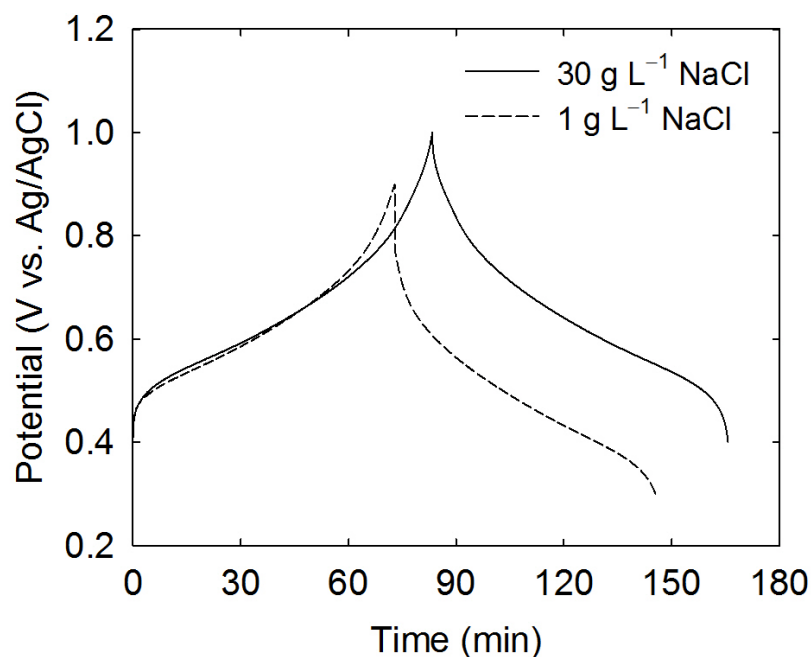


**Figure S16.** Representative galvanostatic charge/discharge profiles of the copper hexacyanoferrate (CuHCF) electrode in 1 and 30 g L<sup>-1</sup> NaCl solutions (constant applied current of 1 mA, area = 7 cm<sup>2</sup>). A different potential range was used for each experiment (0.4 to 1.0 V for 30 g L<sup>-1</sup> NaCl and 0.3 to 0.9 V for 1 g L<sup>-1</sup> NaCl) because the electrode potential was affected by the concentration. The experiment was performed in a 3-electrode cell with Ag/AgCl as a reference electrode and activated carbon as a counter electrode. Discharge capacities were 51.6 mAh g<sup>-1</sup> (699 mC cm<sup>-2</sup>) in 30 g L<sup>-1</sup> NaCl and 45.5 mAh g<sup>-1</sup> (616 mC cm<sup>-2</sup>) in 1 g L<sup>-1</sup> NaCl based on the mass of CuHCF. The coulombic efficiency was 99% for both conditions.

**Table S1.** Comparison of electrochemical systems using seawater

	Potential gain	Electrode	Feed concentration (M)		Power density <sup>a</sup> (W m <sup>-2</sup> )	Ref
			High	Low		
<i>This work</i>	2 electrodes 1 IEM <sup>b</sup>	CuHCF	0.513	0.017	3.76 [12.55]	
CapMix	2 electrodes	CuHCF	0.513	0.017	0.41	4
	2 IEMs	AC <sup>d</sup>	0.513	0.017	0.21	5
	2 electrodes	NMO <sup>e</sup> , Ag	0.6	0.024	0.11	6
	1 electrode 1 IEM	NMO, AC	0.6	0.01	0.1	7
	2 electrodes	Modified AC	0.5	0.02	0.05	8
	2 IERs <sup>c</sup>	AC	0.513	0.017	0.05	9
	2 electrodes	Modified AC	0.5	0.02	0.04	10
	2 IEMs	AC	0.51	0.01	0.03	11
RED	IEMs	Ti-Pt 0.3 M K <sub>3</sub> /K <sub>4</sub> [Fe(CN) <sub>6</sub> ]	0.507	0.017	2.9	12
	IEMs	Platinum clad niobium 0.05 M K <sub>3</sub> /K <sub>4</sub> [Fe(CN) <sub>6</sub> ]	0.58	0.017	2.4	13
	IEMs	Ti-Ru/Ir 0.025 M K <sub>3</sub> /K <sub>4</sub> [Fe(CN) <sub>6</sub> ]	0.507	0.017	2.2	14
	IEMs	Ti-Ru/Ir 0.05 M K <sub>3</sub> /K <sub>4</sub> [Fe(CN) <sub>6</sub> ]	0.507	0.017	1.3	15
	IEMs	AC	0.508	0.017	0.95	16
	IEMs	Ti-Ru/Ir 0.05 M K <sub>3</sub> /K <sub>4</sub> [Fe(CN) <sub>6</sub> ]	0.507	0.017	0.93	17

a number given in brackets is peak power density

b IEM = ion-exchange membrane

c IER = ion-exchange resin

d AC = activated carbon

e NMO = sodium manganese oxide

**Table S2.** Comparison of electrochemical systems using brine

	Potential gain	Electrode	Feed concentration (M)		Power density <sup>a</sup> (W m <sup>-2</sup> )	Ref
			High	Low		
<i>This work</i>	2 electrodes 1 IEM <sup>b</sup>	CuHCF	5.133	0.017	9.39 [26.3]	
RED	IEMs	Ti-Ru/Ir 0.1 M K <sub>3</sub> /K <sub>4</sub> [Fe(CN) <sub>6</sub> ]	5	0.01	6.7 (60°C) 5.3 (40°C) 3.8 (25°C)	18
	IEMs	Ti-Ru/Ir 0.1 M K <sub>3</sub> /K <sub>4</sub> [Fe(CN) <sub>6</sub> ]	5	0.1	6 (40°C)	19
	IEMs	Ti-Ru/Ir 0.3 M K <sub>3</sub> /K <sub>4</sub> [Fe(CN) <sub>6</sub> ]	4-5	0.03	0.8 (natural) 1.35 (artificial)	20

a number given in brackets is peak power density

b IEM = ion-exchange membrane

## Supplementary References

1. C. D. Wessells, R. A. Huggins and Y. Cui, *Nat. Commun.*, 2011, **2**, 550.
2. N. Y. Yip and M. Elimelech, *Environ. Sci. Technol.*, 2012, **46**, 5230-5239.
3. A. J. Bard and L. R. Faulkner, *Electrochemical Methods: Fundamentals and Applications, 2nd Edition*, John Wiley & Sons, 2000.
4. T. Kim, M. Rahimi, B. E. Logan and C. A. Gorski, *Environ. Sci. Technol.*, 2016, **50**, 9791-9797.
5. F. Liu, O. Schaetzle, B. B. Sales, M. Saakes, C. J. Buisman and H. V. Hamelers, *Energy Environ. Sci.*, 2012, **5**, 8642-8650.
6. F. La Mantia, M. Pasta, H. D. Deshazer, B. E. Logan and Y. Cui, *Nano Lett.*, 2011, **11**, 1810-1813.
7. J. Lee, H. Yoon, J. Lee, T. Kim and J. Yoon, *ChemSusChem*, 2017, 10.1002/cssc.201601656.
8. D. Brogioli, R. Ziano, R. Rica, D. Salerno, O. Kozynchenko, H. Hamelers and F. Mantegazza, *Energy Environ. Sci.*, 2012, **5**, 9870-9880.
9. M. Fernández, R. Wagterveld, S. Ahualli, F. Liu, A. Delgado and H. Hamelers, *J. Power Sources*, 2016, **302**, 387-393.
10. M. Marino, O. Kozynchenko, S. Tennison and D. Brogioli, *J. Phys.: Condens. Matter*, 2016, **28**, 114004.
11. B. Sales, M. Saakes, J. Post, C. Buisman, P. Biesheuvel and H. Hamelers, *Environ. Sci. Technol.*, 2010, **44**, 5661-5665.
12. J. Moreno, E. Slouwerhof, D. Vermaas, M. Saakes and K. Nijmeijer, *Environ. Sci. Technol.*, 2016, **50**, 11386-11393.
13. H.-K. Kim, M.-S. Lee, S.-Y. Lee, Y.-W. Choi, N.-J. Jeong and C.-S. Kim, *J. Mater. Chem. A*, 2015, **3**, 16302-16306.
14. D. A. Vermaas, M. Saakes and K. Nijmeijer, *Environ. Sci. Technol.*, 2011, **45**, 7089-7095.
15. E. Güler, R. Elizen, M. Saakes and K. Nijmeijer, *J. Membr. Sci.*, 2014, **458**, 136-148.
16. D. A. Vermaas, S. Bajracharya, B. B. Sales, M. Saakes, B. Hamelers and K. Nijmeijer, *Energy Environ. Sci.*, 2013, **6**, 643-651.
17. J. Veerman, M. Saakes, S. Metz and G. Harmsen, *J. Membr. Sci.*, 2009, **327**, 136-144.
18. A. Daniilidis, D. A. Vermaas, R. Herber and K. Nijmeijer, *Renewable energy*, 2014, **64**, 123-131.
19. M. Tedesco, E. Brauns, A. Cipollina, G. Micale, P. Modica, G. Russo and J. Helsen, *J. Membr. Sci.*, 2015, **492**, 9-20.
20. M. Tedesco, C. Scalici, D. Vaccari, A. Cipollina, A. Tamburini and G. Micale, *J. Membr. Sci.*, 2016, **500**, 33-45.